

<https://doi.org/10.1038/s43247-025-03132-0>

Northward rupture and early afterslip of two graben-bounding normal faults during the 2025 Dingri earthquake of Tibet

Check for updates

Wenbin Xu¹✉, Chengyuan Bai¹, Chuanchao Huang¹, Roland Bürgmann², Baojun Shan¹, Xinjian Shan³, Zhidan Chen¹, Lei Xie¹ & Feng Shi³

The Mw 7.0 Dingri earthquake, the largest documented normal-faulting event in southern Tibet, struck within the NS-trending Dinggye-Xainza Rift system. Here we combine field observations, high resolution optical and synthetic aperture radar imagery and seismic waveforms to determine the three-dimensional coseismic deformation field, coseismic rupture processes and early postseismic deformation mechanisms of the event. We find that the rupture propagated unilaterally northward from the earthquake hypocenter, concurrently activating two graben-bounding faults. The main rupture was concentrated on the Dengmo Co fault causing a maximum subsidence of 3 m and a 25-km-long rupture trace at the surface. The first four-months postseismic deformation is dominated by shallow afterslip, which exhibits spatial overlap with the coseismic slip zone. Our observations provide important insights into the rupture kinematics and strain partitioning within the Dinggye-Xainza Rift, offering a valuable framework for understanding continental extensional tectonics and seismic cycle processes in similar southern Tibet grabens.

On 7 January 2025 at 01:05:16 a.m. UTC, a destructive earthquake with a moment magnitude (M_w) 7.0 and a focal depth of 10 km struck Dingri County in Tibet Autonomous Region of Southwestern China, as reported by the China Earthquake Networks Center (CENC). The epicenter was in the southwest of the Dinggye-Xainza Rift (Fig. 1A, B), which represents part of the graben and half-graben structures in the southern plateau. The focal mechanism solutions from different organizations indicate that this event accommodated crustal extension in east-west direction (Fig. 1B), which is consistent with the widespread upper-plate extension observed within the plateau (Fig. 1A). The earthquake resulted in at least 126 fatalities and 188 injuries in Dingri County and its surrounding areas¹. More than 27,200 buildings were damaged, and 3612 houses collapsed. The earthquake's impact extended at least 200 km away, causing injuries to 13 people in Nepal and minor damage in northern India². After the earthquake, researchers used aftershock relocation, back-projection imaging and finite-fault inversion to determine the fault geometry, slip distribution, and rupture process^{3–7}. Qiao et al., (2025) used Sentinel-1 and Lutan-1 SAR data to analyze the coseismic displacement field of the 2025 Mw 7.0 Dingri earthquake⁶. They found the earthquake ruptured two conjugate normal faults, confirming the east-dipping secondary fault's coseismic slip via relocated aftershocks. Yang et al., (2025) used InSAR data from different satellites (Sentinel-1, Lutan-1, ALOS-2) to analyze coseismic and

postseismic deformation of the 2025 Dingri earthquakes⁷. They found that the 2025 mainshock ruptured on the Dengmo Co fault (DMCF) and generate obvious postseismic signals. However, the existing studies either considered only the rupture process of a single fault or performed static fault inversions³, without accounting for the interaction between the two graben-bounding faults^{5–7}. This event ranks as one of the largest magnitude normal earthquakes documented in the Tibetan Plateau. Therefore, it has the potential to provide important insights into the seismogenic mechanisms and surface rupture patterns of such earthquakes for graben development and regional seismic hazard assessments. It also provides an excellent opportunity to investigate the post-seismic deformation mechanisms over the first four months following the earthquake.

The extensional rifts within the Tibetan Plateau are widely interpreted as a response to north-south crustal shortening by east-west oriented extension^{8–12}. Global Navigation Satellite System (GNSS) measurements and geological studies show that the extension rates across these grabens vary spatially, estimated to add up to about 10–22 mm/year^{10,11}. These extension rates are distributed across seven major rifts (Fig. 1A), with each individual rift absorbing an extension rate of 2–5 mm/year¹³. The large-scale east-west extension is expressed in the brittle upper crust as distinct extensional structures, which have been identified via field surveys and geodetic monitoring^{9,10,13}. These structures are further coupled with ductile

¹School of Geosciences and Info-Physics, Central South University, Changsha, China. ²Department of Earth and Planetary Science and Berkeley Seismology Lab, University of California, Berkeley, CA, USA. ³Institute of Geology, China Earthquake Administration, Beijing, China. ✉e-mail: wenbin.xu@csu.edu.cn

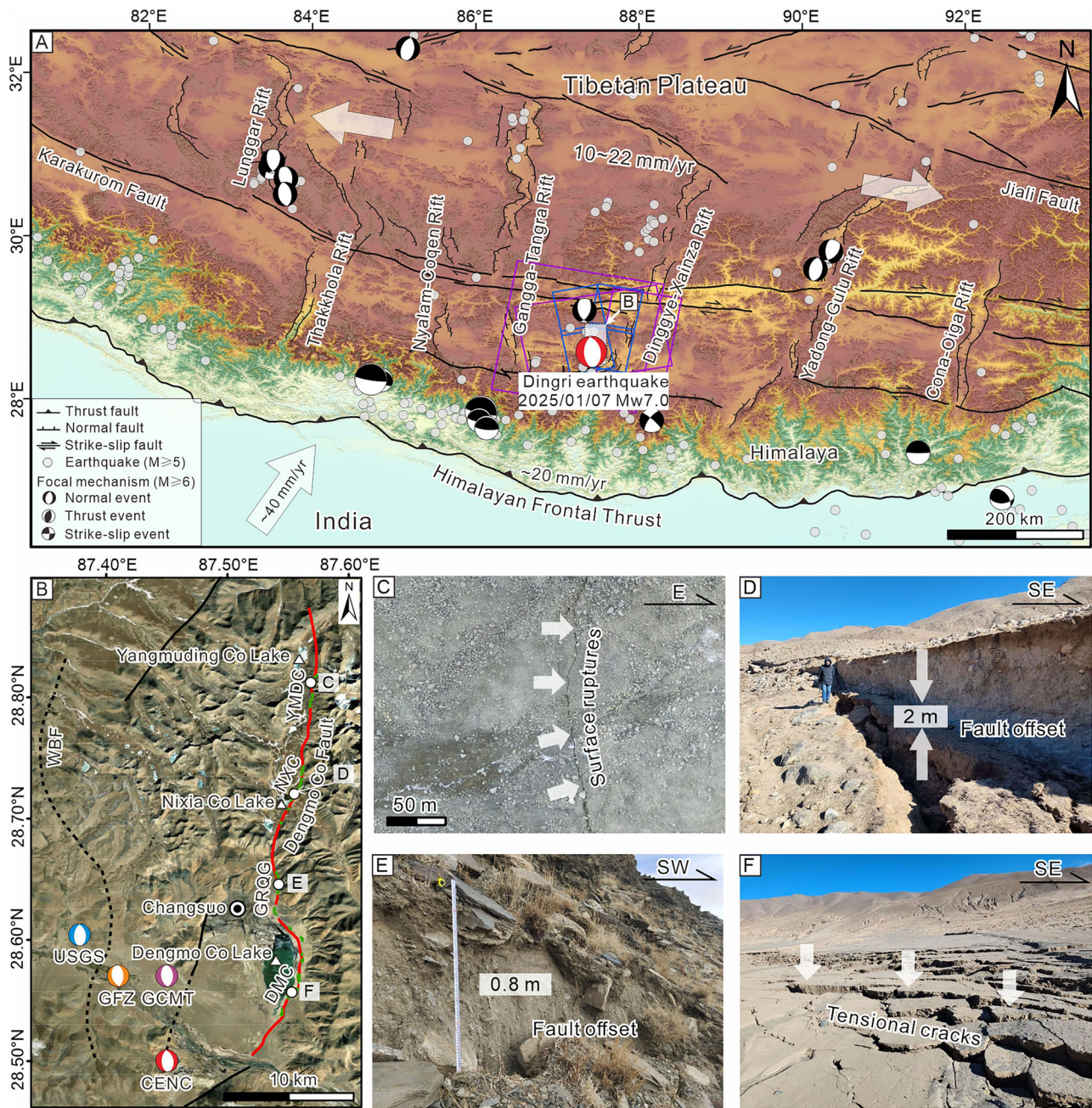


Fig. 1 | Tectonic overview map and mapped surface rupture of the 2025 Dingri earthquake. **A** Tectonic setting of the southern Tibetan plateau showing the regional active faults, extensional rifts, seismicity, and focal mechanisms. The active faults are referenced from Zelenin et al.⁵¹ and Tian and Wu²⁰. The gray dots denote earthquakes ($M \geq 5$) since 1990, with focal mechanisms shown for $M \geq 6$ events. The historical seismic data and focal mechanisms are sourced from the U.S. Geological Survey (USGS). The epicenter and focal mechanism of the Dingri earthquake are from the CENC. Blue and purple rectangles represent the coverage areas of the Lutan-1 and Sentinel-1 SAR satellite data, respectively. White rectangle box in (A) outlines the zoomed-in region of the epicenter shown in (B). **B** Optical satellite imagery (ESRI online map) illustrates the active faults and surface ruptures near the

epicenter, with field evidence (marked with letters) shown in (C–F). Focal mechanisms of the Dingri earthquake are sourced from the USGS, CENC, Global Centroid Moment Tensor (GCMT), GFZ Helmholtz Center for Geosciences (GFZ). Abbreviations: DMC (Dengmo Co segment), GRQG (Gurong-Qiangga segment), NXC (Nixia Co segment), WBF (Western bounding fault), YMDG (Yangmuding Co segment). **C** Unmanned aerial vehicle image shows surface ruptures of the Yangmuding Co segment. **D** Field photograph of the Nixia Co segment shows a vertical displacement of ~2 m. **E** Field photograph of the Gurong-Qiangga segment shows a vertical displacement of ~0.8 m. **F** Tensional surface cracks along the Dengmo Co segment.

flow in the lower crust^{14–17}, creating a vertically heterogeneous deformation system. The geodynamic origins of this E-W extension remain highly contentious, with proposed mechanisms ranging from gravitational collapse⁸ and lateral extrusion¹⁸ to lower crustal flow¹⁵. This debate also extends to how intracontinental deformation mediates critical post-collisional tectonic processes, including crustal shortening and thickening¹⁹ and stress transfer between fault systems^{11,18}.

In this study, we integrate optical satellite imagery, field investigations, synthetic aperture radar interferometry (InSAR), and seismic waveform data to study the surface deformation features, fault geometry and spatio-temporal rupture process of the 2025 Dingri earthquake. We compare our findings with previously published results with the aim to advance the understanding of graben deformation during and following a major event in the Tibetan Plateau.

Results and discussion

Surface ruptures of the 2025 Dingri earthquake

Field investigations conducted immediately after the earthquake and the high-resolution Gaofen (GF) satellite optical imagery (Fig. S1) show significant surface ruptures and ground deformation associated with the Dingri event (Figs. 1B–F and S1) (See Data and Methods). The surface ruptures are found along the previously mapped DMCF, the fault bounding the rift system to the east²⁰. The coseismic ruptures extend north–south for a total length of ~25 km, stretching from east of Dengmo Co Lake in the south to Yangmuding Co Lake in the north¹ (Fig. 1B). These fault traces are also clearly visible in pre-earthquake Gaofen-6 optical satellite imagery (Fig. S1), indicating that the DMCF has been tectonically active since at least the Late Quaternary period.

Both field observations and optical satellite images clearly show the surface ruptures. These ruptures are discontinuous and can be divided into four segments from north to south: the Yangmuding Co, Nixia Co, Gurong-Qiangga, and Dengmo Co segments, each ranging from 3 to 6 km in length and separated by gaps of ~6 km (Fig. 1B). The Yangmuding Co segment is located along the southeastern side of Yangmuding Co Lake, with an overall near-N–S orientation and a total length of about 3 km, showing poor surface expression. High-resolution unmanned aerial vehicle imagery revealed that this segment has numerous surface ruptures and pressure ridges (Fig. 1C). The Nixia Co segment extends along the eastern side of Nixia Co Lake, with an overall NNE orientation and a total length of approximately 6 km (Fig. 1D). This segment exhibits the largest coseismic displacement along the entire surface rupture zone, with a maximum vertical displacement of up to 3 m. The fault plane dips westward at a near-vertical angle, with the western block moving downward relative to the eastern block, indicating predominantly normal faulting. The surface rupture zone is widest near Nixia Co Lake, reaching up to 450 m. The Gurong-Qiangga segment runs along the northeastern side of Dengmo Co Lake, with a total length of about 5 km and a maximum displacement of up to 0.8 m (Fig. 1E). In addition to the surface ruptures, a dense zone of en échelon tension cracks was observed along the Dengmo Co segment on the eastern shore of Dengmo Co Lake. The diffusive crack zone is about 100–300 m wide and extends for 10 km (Fig. 1F).

Coseismic deformation zones seen from LuTan-1 interferograms and Sentinel-1 pixel offset tracking

The LuTan-1 (L-band) interferograms and line-of-sight (LOS) deformation fields show three distinct deformation zones (Figs. 2 and S2) (See Data and Methods). The main coseismic deformation zone is located approximately 15 km north of the epicenter along the DMCF covering an area of 30 km × 10 km. This primary deformation zone is bounded by a ~25 km-long surface rupture trace along the DMCF. The maximum LOS displacement with respect to a reference point outside of the coseismic deformation field is –2.4 m (i.e., away from the satellite) in the ascending orbit and –1.6 m in the descending view direction, respectively. A secondary deformation zone is observed near the epicenter in both interferograms, with a modest LOS displacement of –0.3 m. The deformation fringes in this area are more continuous and concentric in shape, indicating that the fault rupture occurred at depth and did not reach the surface. Additionally, a third deformation zone covering an area of 10 km × 5 km is found ~8 km on the western side of the deformation zone. The maximum LOS displacement is –0.35 m in the ascending orbit. This WBF is bounded to the west by a previously unmapped fault, which defines the regional geomorphic boundary and displays fault-offset features (Fig. 1B). The consistency between ascending and descending deformation patterns indicates predominantly vertical motions characterized by subsidence. The secondary LuTan-1 radar image was acquired within three hours after the earthquake, giving proof that the deformation is mostly co-seismic. The Sentinel-1 pixel offset tracking (POT) results demonstrate excellent consistency with the LuTan-1 interferograms while effectively compensating for the lack of near-field LuTan-1 InSAR observations due to decorrelation (Fig. S3) (See Data

and Methods). The POT analysis reveals significantly larger displacement magnitudes in range direction compared to the azimuth direction, with maximum range offsets of –2.2 m (ascending track 12) and –1.9 m (descending track 121), both located in the near-field region west of the DMCF.

Three-dimensional coseismic ground deformation

We used a least-squares method to resolve the complete three-dimensional coseismic deformation of the 2025 Dingri earthquake using LuTan-1 SAR interferograms and Sentinel-1 pixel offset results²¹ (See Data and Methods). This three-dimensional coseismic deformation field confirms the Dingri earthquake's dominant normal faulting mechanism (Figs. 3A and S4). Vertical displacements show limited subsidence of ~0.4 m near the epicenter, contrasting with pronounced subsidence of ~2.6 m along the DMCF hanging wall extending from the epicenter to 30 km north. The footwall exhibits modest uplift with a maximum of ~0.4 m, collectively forming a half-graben structure (Fig. 3A, B). Interestingly, a secondary deformation gradient emerges along the previously unmapped fault that bounds the graben to the west. It is characterized by ~0.25 m of subsidence. The gradual gradient in vertical motion above the WBF indicates blind fault slip. The pattern of 3D displacements is far from being symmetric across the graben, which is clearly seen when vertical displacements along a profile crossing the graben are plotted (Fig. 3B, C). The profile displacements show up to ~2.1 m vertical offset across the NXC, in agreement with the field-observed displacement of ~2 m (Fig. 1D), while revealing a gradual vertical change to the west, with no large vertical offsets. Horizontal displacement vectors show graben widening through an asymmetric divergent motion, with maximum horizontal displacements of almost 1.9 m across the graben (Fig. 3A). The hanging wall of the DMCF slipped downward along the fault dip, leading to a westward horizontal motion in the near-field rupture zone on the western side of the DMCF. At the same time, the vertical deformation field shows that the amplitude of vertical displacement gradually increases from the eastern side of the WBF to the western side of the DMCF. This differential deformation produces a rotation-like effect, resulting in a pronounced eastward motion in this region.

Fault geometry and rupture kinematics

Guided by the identified surface traces mapped in the field and deformation zones in the coseismic deformation fields, we modeled the Dingri earthquake using two graben bounding faults, designated as DMCF for the eastern graben bounding fault and the western bounding fault (WBF). Based on the grid search results constrained by InSAR observations (Fig. S5), we searched for the depth-dependent dip angles of these two faults (See Data and Methods). The modeled DMCF is a westward-dipping fault, with a dip angle of 60° at the Earth's surface and 32° in the down-dip portion, while the modeled, curved WBF dips eastward with a constant dip angle of 64° (Fig. S6). Once the geometry of the seismogenic fault was determined, we jointly inverted the InSAR and seismic wave observations for the kinematic coseismic fault slip distribution. The teleseismic data were downloaded from the Incorporated Research Institutions for Seismology (IRIS). We selected vertical component velocity records (BHZ) from 32 broadband stations with epicentral distances ranging from 30° to 90° (Fig. S7). The time window for extracting the direct P waves was from 20 s before the P-wave arrival to 80 seconds after the P-wave arrival. The frequency band used for filtering was 0.01–0.15 Hz (Fig. S8). The modeling results show a good agreement between the predicted ground deformation and seismic waveforms and the observations (Fig. 2). The average correlation coefficient of the seismic waveforms is 0.9, and the RMS misfit of the coseismic LuTan-1 data is 5 cm. The residuals are likely due to atmospheric effects and the model simplifications, such as the assumption of a single planar fault and a smoothed slip distribution.

The kinematic fault model reveals that the earthquake rupture propagated unilaterally northward along the DMCF from the hypocenter at a depth of approximately 11 km, which marks the southernmost tip of the Dinggye-Xainza graben (Figs. 4A and S9). The slip along the DMCF is

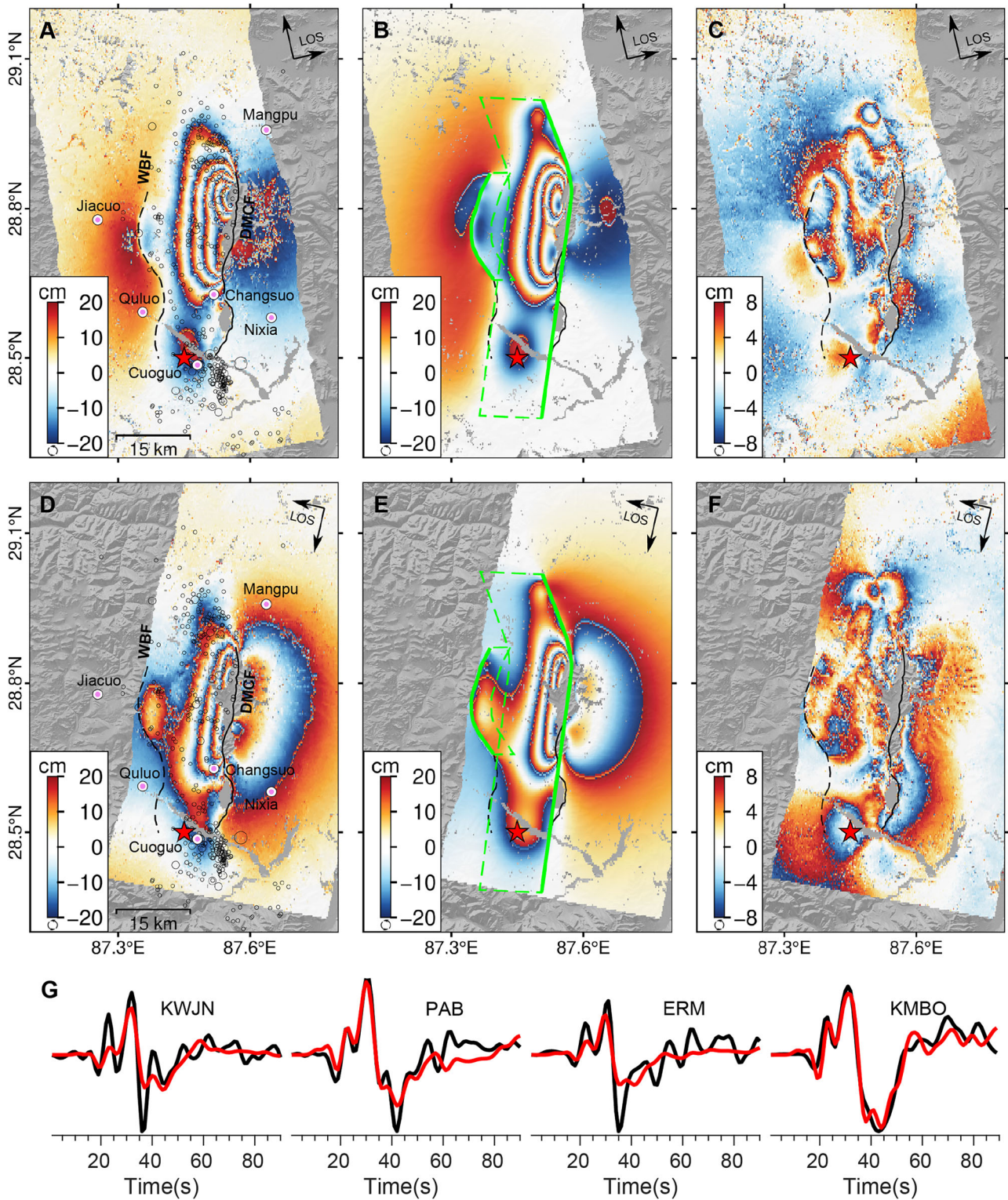


Fig. 2 | Coseismic LuTan-1 InSAR data of Dingri earthquake and the modeling result. **A** Coseismic surface deformation in ascending orbit. Each color cycle represents 40 cm of line-of-sight (LOS) displacement toward (blue-white-red) or away from (red-white-blue) the satellite. Red star represents the epicenter (CENC) of the Dingri earthquake, black solid lines indicate active faults²⁰. Black circles represent early aftershocks that occurred between January 7 and January 18, 2025. **B** Predicted

co-seismic displacements with the surface projection of the modeled fault plane indicated by green rectangles (upper edge in bold). **C** Residuals. Each color cycle represents 16 cm of LOS displacement. **D–F** same as (**A–C**), but for the descending orbit. **G** Teleseismic body waveforms and the model fitting. Black lines represent the observed waveforms. Red lines represent the synthetic seismograms generated by the best-fitting model.

Fig. 3 | Three-dimensional coseismic displacement field. A 3D deformation field derived from Lutan-1 and Sentinel-1 satellite imagery. Arrows represent horizontal displacement; color indicates vertical motion. Red star indicates the epicenter. Green line represents the surface trace of the inverted fault model. Purple triangles denote field photo positions shown in Fig.1 C-F. B, C Vertical displacements vs topography (shaded gray) along profiles perpendicular and parallel to the causative faults³.

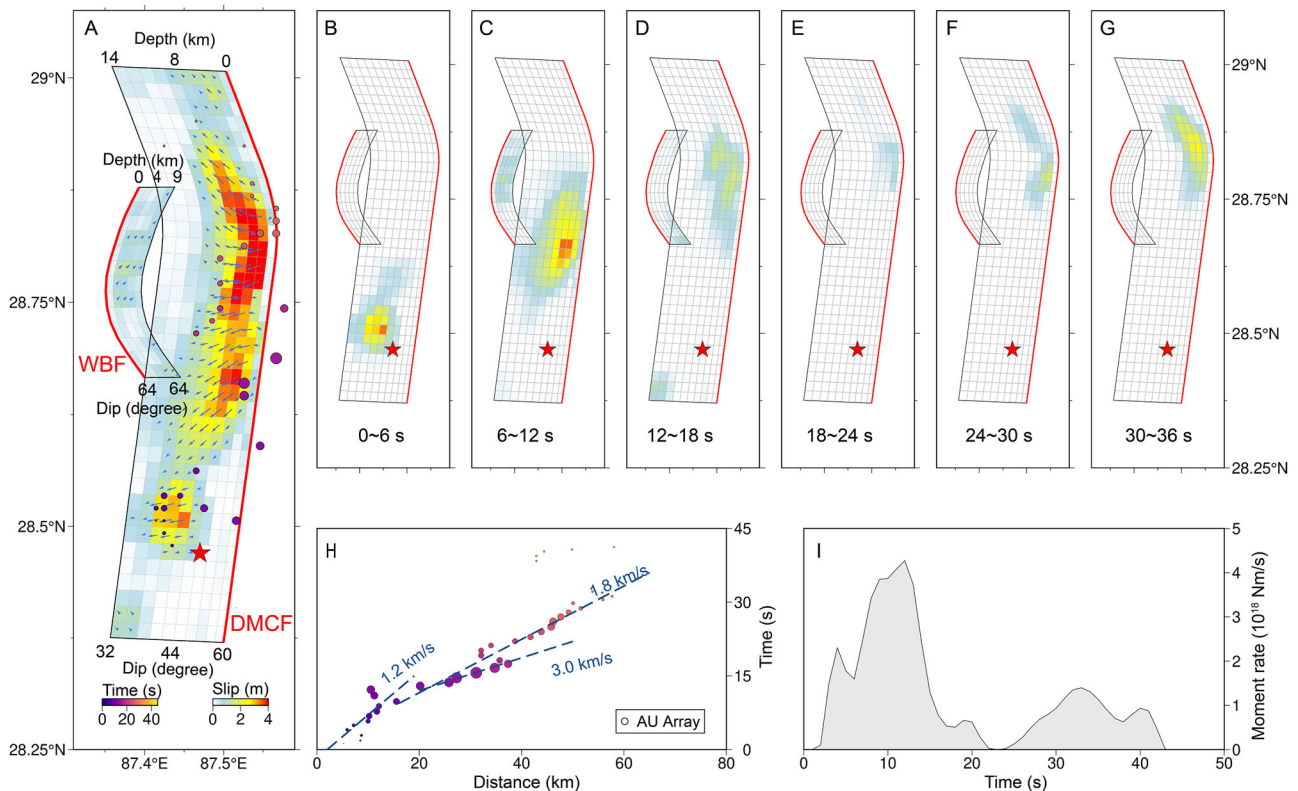
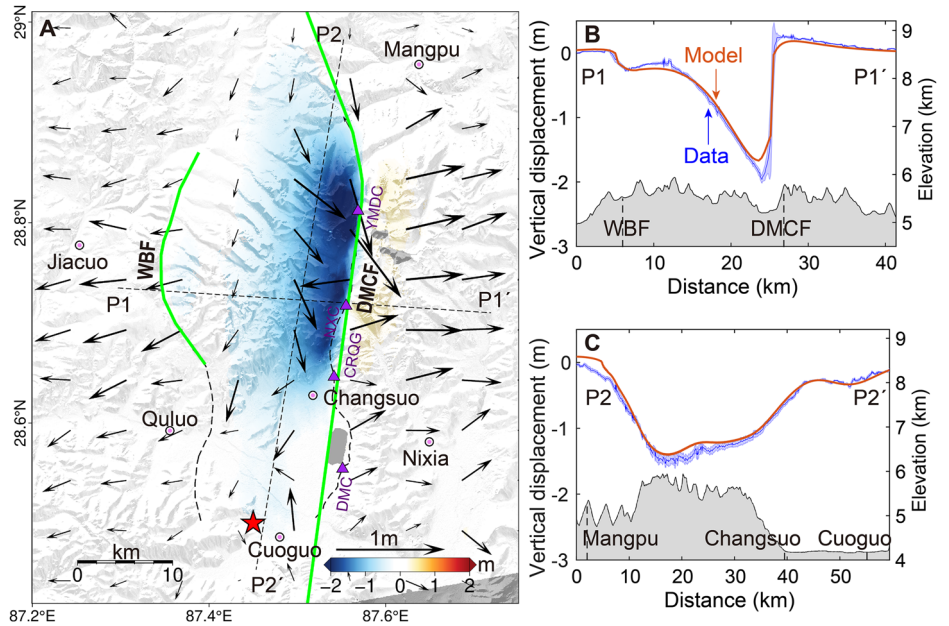


Fig. 4 | Kinematic fault rupture process. A Kinematic fault slip model of the 2025 Dingri earthquake. The colored circles indicate back-projection results using the Australian array, with the size corresponding to the energy distribution. Red line denotes the top of the fault. Red star represents the epicenter. Blue arrows show the slip direction on each subfault patch. B–G Snapshots of cumulative slip for 6 s-time

windows during the first 36 s of rupture. H Distance-time plot from back-projection analysis, with the positive direction representing the propagation from the epicenter along the fault toward the northeast. I The moment rate function obtained from the rupture process inversion.

mainly concentrated around and to the north of the hypocenter, showing good agreement with the surface observations. The first 6 s of rupture were confined to the vicinity of the source region (Fig. 4B). As the rupture propagated northward along the DMCF, it encountered a strong barrier approximately 9 km × 9 km in size at a depth of 10 km (Fig. 4C). This barrier

results in relatively subtle surface deformation above it. Once the rupture bypassed the barrier, it accelerated northward and triggered the failure of the primary asperity at 6–12 s, located approximately 20 km north of the epicenter, with a maximum slip of 4.1 m. Meanwhile, the WBF also ruptured during this period, with a slip of ~1 m (Fig. 4C). As the rupture continued

northward along the DMCF, it nearly stopped at a bend of the fault 23 s after the rupture began. After 24 s, this barrier was breached, and the largest asperity was located at the geometric bend, with a slip of 4.3 m (Fig. 4D–G). The moment rate function indicates that the energy release rate was nearly zero at 23 s, with three distinct peaks corresponding to rupture of the three main asperities. The rupture was predominantly concentrated along the eastern normal fault, resulting in a roughly 25 km-long surface rupture with a maximum surface displacement of 3.0 m, consistent with the field observations. Assuming a shear modulus of 30 GPa, the total energy release is equivalent to an Mw 7.1 earthquake, with the WBF contribution equivalent to an Mw 6.3 earthquake (Fig. 4I). The higher moment magnitude estimate, compared to the seismically derived Mw 7, is possibly due to the inclusion of the first three hours of postseismic deformation in the LuTan-1 data.

A seismic back-projection from an Australian array results indicate that the rupture primarily occurred in two stages (Fig. 4H). The first stage, spanning the initial 7 s, involved a slow northward rupture propagation near the source region (1.2 km/s to 1.8 km/s). The second stage, starting ~10 s after the earthquake began, saw the rupture accelerate (1.8 km/s to 3.0 km/s). We observed a relatively strong energy peak in the back-projection around 24 s, which corresponds to an asperity near a geometric bend along the DMCF.

Early postseismic deformation

The largest cumulative postseismic displacements spanning the first four months following the mainshock were observed in the near-field region of the DMCF. Specifically, the ascending track recorded maximum displacement of –6 cm in LOS on the western side of the northern rupture terminus, whereas the descending track showed ~8 cm of LOS displacement on the eastern side of the central rupture segment (Fig. 5). The postseismic 2D deformation field, derived by ignoring the north–south component, shows that the east–west displacements exhibit a broader spatial distribution compared to vertical displacements (Fig. S10), with a pattern similar to the coseismic east–west displacement field. A significant subsidence zone of ~6 cm is bounded by the WBF, indicating that the underlying deformation takes place in the shallow crust (Fig. S10). Localized deformation signals are also observed at both the northern and southern ends of the rupture. The northern signal may reflect postseismic deformation on nearby faults triggered by coseismic stress changes, whereas the ~5 cm in LOS signal at the southern end is likely associated with aftershock activity associated with an M5.0 earthquake in the region on January 13, 2025 (CENC) (Fig. 5A, B).

Based on the observed postseismic deformation (Figs. 5 and S11), we modeled poroelastic rebound, viscoelastic relaxation, and kinematic afterslip to investigate the dominant mechanism governing the early postseismic deformation following the Dingri earthquake. The modeling results indicate that the deformation predicted by poroelastic rebound substantially differs from the observations in both spatial distribution and magnitude (Fig. S12). The viscoelastic relaxation effectively recovers long-wavelength deformation signals but significantly underestimates near-field displacements (Fig. S13). Compared with the pure afterslip model, the afterslip model accounting for contributions from viscoelastic relaxation reduces the maximum afterslip on the DMCF and WBF by 35% and 53%, respectively, and decreases the RMS misfits by 12% and 24% for the ascending and descending orbits, respectively (Figs. S14–S16). Residual displacements in the near-field regions may reflect unmodeled complex fault geometry. In our preferred combined viscoelastic–afterslip model, afterslip dominates most near-field deformation. The DMCF afterslip primarily occurs updip of the coseismic rupture, with maximum slip (~0.32 m) located at 0–2 km depth near the southern terminus (Figs. 5E and S17). The WBF afterslip concentrates in shallow regions, peaking at ~0.14 m. The depth distribution of afterslip on the WBF is partially overlapped with the coseismic slip. The total moment released by postseismic afterslip is equivalent to Mw 6.2. However, due to the lack of Sentinel-1 observations during the first few days after the earthquake, this result may be underestimated.

Synchronous unilateral rupture of graben-bounding normal faults

Our kinematic fault slip model shows that the 2025 Dingri earthquake resulted in concurrent rupturing along the two normal faults bounding the Dinggye-Xainza graben. The coseismic moment release is predominantly concentrated on the eastern bounding fault, accounting for approximately 93% of the total released energy. The early aftershock catalog from the CENC indicates only one aftershock of magnitude ~4.3 near the western deformation zone within the same timeframe⁴, which is insufficient to explain the observed surface deformation along the WBF, with a vertical displacement of ~0.25 m, corresponding to an estimated moment release equivalent to a Mw 6.3 subevent on the WBF. Given that the slip on the WBF reached 1 m within three hours after the mainshock, while only 0.14 m occurred over the subsequent four months, it is unlikely that afterslip on the WBF could reach such a high magnitude that it should have radiated energy. This suggests that the deformation zone bounded by the WBF was not caused by an aftershock or aseismic afterslip but rather by the mainshock itself. As the rupture propagated northward along the DMCF, it triggered failure of the WBF via stress interaction. The co-rupture of these two faults generated the observed coseismic deformation fields. This highlights the need to assess not only the seismic potential of primary faults but also that of surrounding secondary faults. It is worth noting that around 20 s after the event nucleated, the rupture nearly stopped at a geometric bend approximately 40 km north of the epicenter. The Coulomb stress calculations also indicate that the slip distribution during the first 20 s imposed stress loading on the region north of the bend (Fig. S18). This might be due to a geometry-related barrier hindering the rupture propagation, which was eventually breached under the combined effect of dynamic and static stress, resulting in slip of about 4 m on the north of it.

Spatially complementary coseismic slip and early afterslip

Consistent with previous studies^{3,6}, the coseismic slip of the Dingri earthquake exhibits a pronounced shallow slip deficit (SSD). SSD, defined as a significant reduction or absence of coseismic slip in the uppermost crust, has been widely documented for many earthquakes^{22–24}. One explanation for SSD is that velocity-strengthening regions in the shallow crust impede the upward propagation of coseismic rupture, implying that SSD can be compensated by shallow interseismic creep or postseismic afterslip^{25,26}. In addition, inelastic deformation occurring in the off-fault damage zone may also contribute to an overestimation of SSD^{23,27}. While Xu et al.²⁸ note that limited near-field constraints may overestimate SSD, this alone cannot account for the large SSD here. The interseismic velocity field reveals no significant discontinuities across the DMCF that could be attributed to shallow creep^{3,13}, suggesting that the SSD is unlikely to be accommodated by interseismic creep. Our afterslip model shows that shallow afterslip within the first four months recovered ~10% of the SSD. Although this estimation may be underestimated due to the absence of deformation data from the first few days after the earthquake, the lack of shallow coseismic slip likely also involves contributions from inelastic deformation near the fault zone^{22,23}. In addition, the coseismic rupture is inferred to have nucleated at a depth of approximately 11 km and primarily propagated northward rather than upward. As a result, a shallow coseismic slip gap is present between the hypocenter and the maximum-slip zone to the north. Both the magnitude of afterslip and the number of aftershocks in this region are limited compared to other portions of the fault plane (Fig. 5E), and this area is located within the coseismic Coulomb stress loading zone (Fig. S18), suggesting a potentially elevated seismic hazard in the future.

The spatial distribution of seismic and aseismic slip provides valuable insights into the frictional properties of faults²⁹. In the case of the Dingri earthquake, coseismic slip, afterslip, and aftershocks exhibit a clear spatial complementarity (Fig. 5E). Early postseismic afterslip is primarily distributed within the 0–10 km depth range, particularly up-dip of the coseismic rupture, in a zone of reduced coseismic slip. Relocated aftershocks within 11 days following the mainshock are mainly concentrated at the

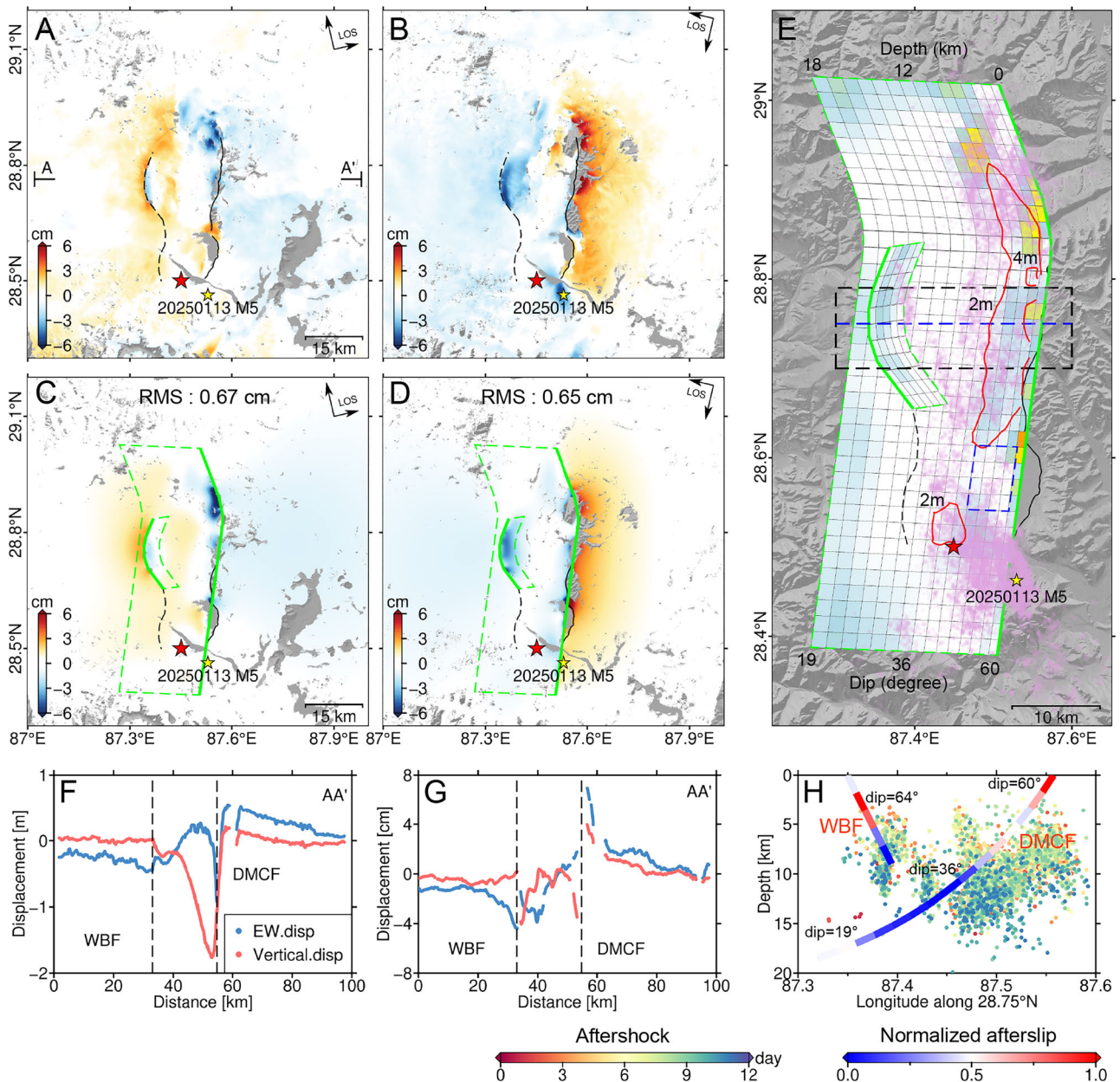


Fig. 5 | Cumulative postseismic deformation over four months after the mainshock and the combined viscoelastic relaxation and afterslip model (VR + AS). A, B represent the ascending and descending postseismic Sentinel-1 InSAR observations, respectively. Red star represents the epicenter of the mainshock. Yellow star marks the M5.0 aftershock that occurred on January 13, 2025 (CENC). C, D represent the corresponding VR + AS model predictions. E Afterslip model after accounting for contributions from viscoelastic relaxation. Red contours represent the spatial distribution of coseismic slip in 2 m interval. Purple circles represent relocated aftershocks within 11 days after the mainshock^{4,30}. Green solid

lines indicate the surface traces of the fault model. Blue dashed box highlights the fault region with elevated seismic potential. F Coseismic displacements along profile AA', with east–west and vertical components shown as blue and red lines, respectively. The location of AA' is indicated in (A). G Cumulative postseismic displacements along profile AA'. H A depth profile across the seismogenic faults. Colored circles represent the projection of aftershock data from the black dashed box in (E) onto this depth profile, with colors denoting the time elapsed since the mainshock. The DMCF and WBF fault sections are colored according to the normalized results of their average afterslip at different depths.

northern and southern ends of the rupture, with most events terminating at a depth of around 15 km^{4,30} (Fig. 5E and H). They are also found in areas surrounding zones of large coseismic slip, where coseismic slip is low. Such spatial complementarity between seismic and aseismic slip and aftershocks implies that the Dinggye–Xainza Rift fault zone might contain considerable fine-scale structural and frictional heterogeneity, including sections that have velocity strengthening properties favoring aseismic slip. Continued tracking and frictional modeling of the evolution of afterslip will help further explore the varied mechanical properties of the rift bounding faults. Furthermore, long-term viscoelastic relaxation modeling will better constrain

the lower-crustal viscosity structure, providing valuable constraints for geodynamic studies.

Implications for present tectonics within the southern Tibetan rift system

The heterogeneity of extensional deformation in the southern Tibetan Plateau poses a control on the deformation pattern observed during the 2025 Dingri earthquake. Current studies indicate that the extension rate of the South Tibetan Rift System (10–22 mm/yr) is approximately equivalent to the Himalayan Frontal Thrust’s convergence rate (15–20 mm/yr)^{13,31–33}.

However, the extension rate decreases from the central plateau toward the southern margin^{11,31,34}, leading to heterogeneous strain accumulation within the Tibetan grabens. Consequently, the northward increase in strain accumulation and extension rate within the Dinggye-Xainza graben resulted in significantly greater coseismic deformation in the northern section of the Dingri earthquake compared to the south. Additionally, the observed 1.9 m left-lateral strike-slip in line with other observations³⁻⁶, and the widespread oblique slip collectively indicates the rift system does not undergo pure E-W extension, but a mixed kinematic regime³⁵. Furthermore, InSAR data reveal that the earthquake ruptured only the northern segment of the DMCF, with no significant surface rupture detected on the southern segment, suggesting independent segment-bounding rupture behavior within the rift system.

Conclusions

We present a comprehensive analysis of the three-dimensional deformation field, rupture processes and early postseismic deformation of the Mw 7.0 Dingri earthquake through field observations, high-resolution optical and radar imagery, and seismological data. We show that the coseismic ground deformation was characterized by predominantly vertical subsidence with a sinistral strike-slip component. We find a maximum displacement of ~3 m observed along the hanging wall of the west-dipping DMCF. We find the coseismic rupture initiated near the hypocenter on the DMCF, the earthquake's dominant fault, propagated unilaterally northward, and triggered the concurrent activation of two graben-bounding faults. We also find that postseismic observations during the first four months were concentrated near the ruptured faults and were primarily driven by shallow afterslip, which is spatially complementary to coseismic slip. These observational constraints demonstrate that the preferred postseismic model includes both afterslip and viscous relaxation, as neither mechanism alone can fully reproduce the observed deformation signal. The coseismic deformation pattern and early postseismic afterslip reveal heterogeneous strain accumulation within the Tibetan extensional grabens and potentially high seismic hazards in the southern plateau.

Data and methods

High resolution Gaofen optical images

We used optical images from Gaofen (GF) satellite constellation to visually trace the co-seismic surface ruptures. The 2-m panchromatic resolution of GF-6 image, acquired on December 15, 2024 (23 days before the mainshock), was used as a reference for the pre-earthquake existing surface ruptures (Table S1). A GF-1C image with a 2-m resolution acquired four hours after the main events (at 04:14 UTC), and a GF-2 image with a 0.8-m resolution acquired on January 8 (1 day after the mainshock) were employed to delineate the new rupture traces. These fault scarps and ground cracks were manually identified and traced to define the complete surface rupture geometry. All the images were preprocessed with radiometric calibration and geometric correction using the ENVI and QGIS software.

Coseismic InSAR data processing

We used L-band (wavelength of 23.8 cm) LuTan-1 SAR data (Table S2) acquired through the Natural Resources Satellite Remote Sensing Cloud Service Platform to map full-coverage coseismic deformation from the Dingri earthquake. LuTan-1 is China's first L-band fully-polarized satellite constellation³⁶. Compared to C-band (wavelength of 5.6 cm) Sentinel-1 observations, the longer wavelength of LuTan-1 demonstrated better coherence preservation in near-field fault regions, significantly enhancing the surface deformation characterization. For ascending track analysis, we processed SAR images from December 6, 2024, and January 7, 2025. Notably, LuTan-1 achieved good post-earthquake monitoring capability by imaging the affected area within three hours of the mainshock. For the descending track, data acquisitions occurred on November 14, 2024, to January 9, 2025, including two days of postseismic deformation.

The LuTan-1 data were acquired in stripmap mode and processed using Differential Interferometric Synthetic Aperture Radar in GAMMA software to obtain the LOS coseismic deformation fields^{37,38}. The

interferograms were multilooked by 2 and 5 looks in range and azimuth directions to improve the signal-to-noise ratio (SNR). The topographic phase in the interferograms was calculated and removed using the one-arc second resolution Shuttle Radar Topography Mission (SRTM) Digital Elevation Model (DEM)³⁹, which was acquired in 2000 by spaceborne radar interferometry and provides near-global coverage with ~30 m spatial resolution. Goldstein filtering was first applied to interferograms⁴⁰. Areas with coherence below 0.3 or discontinuous fringes were masked. Phase unwrapping was then performed using the minimum cost flow method⁴¹, and the unwrapped interferograms were finally geocoded into a geographic coordinate system. Apparent phase unwrapping errors in the near-field were manually masked out from the ascending and descending unwrapped interferograms, respectively. A second-order polynomial fit was applied to derive a long-wavelength ramp due to inaccurate orbits and ionospheric noise, which was then removed from the observation data (Fig. S2).

Pixel offset tracking processing

Due to the large coseismic deformation caused by this earthquake, the interferograms generated from Sentinel-1 SAR images (Table S2) exhibit significant decoherence in the near-field region. Therefore, we only used Pixel Offset Tracking (POT) to obtain the near field range and azimuth coseismic deformation field^{38,42}. POT calculates the displacement of each pixel by conducting a cross-correlation search across the images. We obtained Sentinel-1 SAR image data from three tracks through the Alaska SAR Facility (ASF) platform (<https://search.asf.alaska.edu>). The ascending track data (path 12) were acquired on January 5, 2025, and January 17, 2025. The descending track data consist of two tracks: path 48, with image acquisition on December 27, 2024, and January 8, 2025, and path 121, with image acquisition on January 1, 2025, and January 13, 2025. We used SRTM DEM for precise co-registration of the SAR images, with a search window size set to 256×256 pixel in the POT analysis. After obtaining the POT deformation results, we applied a median filter with a window size of 15 pixels to suppress noise and improve the quality of the deformation results. The precision of the POT results is directly related to the pixel resolution. For Sentinel-1 images, the displacement accuracy in the range direction (~2.3 m resolution) is higher than in the azimuth direction (~14.0 m resolution). As a result, the uncertainty of the azimuth offset is an order larger. The mean standard deviation of the range deformation field is 4.7 cm, whereas that of the azimuth deformation field is 9.6 cm (Table S3).

Three-dimensional deformation decomposition

After obtaining all the deformation fields, we inverted the three-dimensional deformation field based on the imaging geometry of the SAR images²¹. The relationship between LOS deformation and azimuth deformation for the respective data, and the three-dimensional deformation is as follows:

$$D_{los} = -D_e \cos(\alpha) \sin(\theta) + D_n \cos(\alpha) \sin(\theta) + D_u \cos(\theta) \quad (1)$$

$$D_{azi} = D_e \sin(\alpha) + D_n \cos(\alpha) \quad (2)$$

In Eqs. (1–2), D_{los} is the LOS deformation, D_{azi} is the azimuth deformation, and D_e , D_n , and D_u represent the east-west, north-south, and vertical deformations, respectively. α and θ are the satellite flight azimuth and incidence angle at a given pixel, respectively. We used a least-squares method to calculate the three-dimensional displacement components at each pixel.

Fault geometry

The fault geometries of the eastern bounding DMCF and the western bounding WBF are determined using a grid search approach constrained by the LuTan-1 observations. To enhance computational efficiency, a quadtree downsampling method⁴³ was first applied to the coseismic deformation data before modeling (Fig. S5). For each quadtree square, the difference between all data points within the square and their mean value is calculated. If the difference exceeds 0.03 m, the square is further subdivided into four smaller

parts. Otherwise, the mean value is assigned to the center of the square. The minimum grid size is 0.8 km × 0.8 km. After quadtree downsampling, the number of sampling points is 1357 for the ascending track and 1138 for the descending track of the LuTan-1 data. For the modeling, we used a single rectangular dislocation with uniform slip⁴⁴ to invert the interferograms, assuming a homogeneous, isotropic elastic half-space (Poisson's ratio $\nu = 0.25$). Considering that the strike angles and fault locations can be well-constrained by satellite data and field observations, we only search for the depth-dependent dip angles of these two faults (Fig. S6). We first search for the dip angles of the DMCF, allowing the top and bottom dip angles to vary independently. The dip angles along the remainder of the fault plane follow a linear decrease with depth:

$$\beta = (\varphi_{bottom} - \varphi_{top})/W \quad (3)$$

$$\varphi_z = \varphi_{top} + \beta \times h_z \quad (4)$$

Where β represents the dip angle variation rate along the fault plane, φ_{top} and φ_{bottom} denote the top and bottom dip angles, respectively. W characterizes the along-strike width of the fault plane, while φ_z indicates the local dip angle at depth z . The h_z corresponds to the up-dip distance from depth z to the fault top boundary. The inversion is performed using the steepest descent method⁴⁵, and the root-mean-square (RMS) misfit between the model and observations is used as the evaluation metric (Eq. 5).

$$RMS = \sqrt{\left(\sum_{i=1}^N (d_i^{obs} - d_i^{model})^2\right)/N} \quad (5)$$

Where N is the number of observation points, d_i^{obs} and d_i^{model} represent the observed and modeled deformation at the i -th point, respectively.

Once the fault geometry of the DMCF is determined, we invert for the coseismic deformation based on this fault geometry and subtract the modeled deformation from the InSAR observations. The residual deformation near the WBF is then used to determine the optimal dip angle of the WBF through a best-fitting search approach. Due to the limited constraint provided by InSAR observations on the WBF, its dip angle is assumed to be constant.

Kinematic rupture process simulation, slip distribution and back projection analysis

To simulate the time-dependent kinematic earthquake rupture process, it is necessary to collect seismic data, which can provide important information about seismic wave propagation, earthquake source characteristics, and crustal structure. This information is crucial for understanding and simulating the earthquake rupture process. To reveal the kinematic rupture process of the 2025 Dingri earthquake, we adopted the fixed double-fault geometry model and jointly inverted the InSAR LOS deformation and teleseismic waveforms using the joint inversion method⁴⁶. This method employs linear inversion to obtain the slip amplitude, rake, rupture initiation time, and rise time for each subfault by minimizing the misfit between the simulated and observed values. The objective function was solved using the least squares method. The maximum rupture rise time for a single subfault was set to 25 s. To ensure the physical plausibility of rupture on the double-fault model, we computed the earliest possible rupture initiation time of the WBF based on the maximum allowable rupture velocity and the distance between the WBF subfault and the hypocenter, thereby enabling the simultaneous inversion of both faults. The fault was divided into subfaults of 2 km × 2 km. The maximum allowed rupture velocity was set to 3.5 km/s. To ensure the stability of the inversion results, we applied spatial and temporal smoothing constraints and determined the optimal spatial smoothing factor and temporal smoothing factor, which are 120 and 120, respectively, using the L-curve method (Fig. S19). Finally, we obtained the kinematic rupture process and slip distribution of DMCF and WBF. The Jackknife resampling method was used to assess the uncertainty of the

coseismic slip model⁴⁷. In this process, 80% of the dataset was randomly selected for each inversion, repeated 200 times, and the standard deviation for each subfault was calculated to determine model uncertainty (Fig. S20). The shallow slip deficit for the slip model is evaluated according to the following expression:

$$SSD = (slip_{max} - slip_{up})/slip_{max} \quad (6)$$

Where $slip_{max}$ denotes the maximum value of the average slip at different depths, while $slip_{up}$ represents the average slip in the uppermost crust.

Back projection (BP) is a station processing technique based on the similarity of seismic waveforms from the same station array⁴⁸. Because it requires little prior information such as fault geometry and rupture velocity, it can effectively reveal the characteristics of the rupture kinematics, including rupture direction, rupture velocity, and high-frequency energy release. Considering that the station array located in the rupture direction of the source provides better constraints on the rupture process, we selected the Australia (AU) array to the southeast of the source, with a teleseismic distance between 30° and 90° to avoid the influence of strong depth phases. We analyzed 134 broadband seismograms from the AU array provided by the Incorporated Research Institutions for Seismology. Using the MUSIC BP method⁴⁸, we performed rupture process imaging by aligning the P-wave arrivals with a four-step band-pass filtering from low to high frequencies, based on the source location of the 2025 Dingri earthquake provided by the China Earthquake Networks Center.

Postseismic SAR data processing

In the GAMMA software package³⁷, the SBAS-InSAR method⁴⁹ was used to process Sentinel-1 data (Table S4) spanning four months after the earthquake to obtain early postseismic displacement time-series. As one of the most widely used time-series InSAR techniques, SBAS-InSAR primarily derives deformation time series from interferometric pairs with short temporal and spatial baselines. Here, after constraining the spatial baseline to 200 m, 45 interferograms from the ascending track and 34 from the descending track were generated. During data processing, multi-looking was applied to the SAR images with 20 looks in range and 4 looks in the azimuth direction. The topographic phase was simulated and removed using the one-arc second SRTM DEM³⁹. After phase filtering and unwrapping of the interferograms, interferograms with significant unwrapping errors (i.e., phase closure values exceeding 1.5 rad) were excluded based on the phase closure⁵⁰ results, and pixels with obvious unwrapping errors were masked. The topography-correlated atmospheric effects were corrected using GACOS⁵¹, which is a GNSS-based Generic Atmospheric Correction Online Service that provides high-resolution tropospheric delay maps derived from numerical weather models and interpolation of GNSS data. The turbulent atmospheric effects were suppressed using spatiotemporal filtering with a time window of 30 days and a spatial window of 2 km. Finally, we derived four months of postseismic cumulative displacement through time series analysis.

To further analyze the kinematic characteristics of postseismic deformation, based on the cumulative deformation over four months after the earthquake and ignoring the north-south deformation (since InSAR is effectively insensitive to north-south deformation), the east-west and quasi-vertical deformations were estimated using a weighted least squares inversion:

$$\begin{cases} D_{los_asc} = -D_e * \sin(\theta_{asc}) * \cos(\alpha_{asc}) + D_u * \cos(\theta_{asc}) \\ D_{los_desc} = -D_e * \sin(\theta_{desc}) * \cos(\alpha_{desc}) + D_u * \cos(\theta_{desc}) \end{cases} \quad (7)$$

Where D_{los_asc} and D_{los_desc} represent the cumulative deformation measurements acquired from Sentinel-1 ascending and descending orbits, respectively. The corresponding incidence angles are denoted as θ_{asc} and θ_{desc} for ascending and descending tracks, while α_{asc} and α_{desc} indicate their respective azimuth angles.

Postseismic deformation modeling

Large earthquakes induce stress perturbations that trigger diverse postseismic processes, including afterslip on fault planes, poroelastic rebound in the shallow crust, and viscoelastic relaxation in the lower crust and upper mantle^{52–54}. Here, we employed the coseismic rupture model as the driving source to simulate poroelastic rebound and viscoelastic relaxation, while the afterslip distribution was obtained from kinematic afterslip inversion.

Poroelastic rebound arises from coseismic fault slip that instantaneously alters the pore pressure within crustal aquifers. Following the earthquake, pore fluids migrate from high-pressure regions to low-pressure regions until hydraulic equilibrium is reestablished, resulting in observable surface deformation. This process is typically modeled by assigning different Poisson ratios to represent the contrasting pore pressure states before and after the earthquake^{52,55}. Specifically, coseismic deformation is forward modeled using two different Poisson ratios, and the difference between the two results is interpreted as the surface deformation due to poroelastic rebound. For simplicity, we set the Poisson ratio to 0.25 for the undrained state and 0.21 for the drained state to estimate the total surface deformation pattern associated with poroelastic rebound (Fig. S12).

Viscoelastic relaxation represents the response of the viscous lower crust and upper mantle to the stress changes induced by earthquakes^{53,54}. Given the long timescales over which viscoelastic relaxation operates, it is difficult to effectively constrain the regional viscosity using only four months of postseismic observations. Therefore, we adopt the viscosity values for southern Tibet inferred from previous studies of the 2015 Nepal earthquake to fix the background viscosity^{56–58}. Table S5 demonstrates that previously published viscosity estimates for the lower crust and upper mantle beneath southern Tibet are largely consistent. Using the upper and lower bounds of these reported viscosities, we simulated the postseismic deformation of the Dingri earthquake and found that the resulting difference in predicted peak deformation was only about 2–3 mm. Therefore, we adopted an intermediate viscosity value. It should be acknowledged that adopting the rheological structure and viscosities inferred from the postseismic response of the 2015 Nepal earthquake as prior constraints for the Dingri viscoelastic model introduces inherent uncertainties, as the lithospheric rheology of the two regions may not be identical. Consequently, the resulting viscoelastic relaxation model is intended to capture the first-order characteristics of the postseismic deformation.

Finally, the viscoelastic relaxation model includes two relaxing layers; a viscoelastic lower crust (25–70 km) and a viscoelastic upper mantle (70–200 km), below a 25 km-thick elastic lid. The transient and steady-state viscosities of the lower crust are 3×10^{17} Pa·s and 3×10^{18} Pa·s, respectively, while the steady-state viscosity of the upper mantle is 1×10^{20} Pa·s⁵⁶. We then use the PSGRN/PSCMP code⁵⁹ to simulate the surface deformation associated with viscoelastic relaxation under this background rheology and evaluate its contribution to the postseismic deformation of the Dingri earthquake (Fig. S13). The elastic crustal structure parameters, including P-wave velocity, S-wave velocity, and density, are derived from the Crust1.0 model⁶⁰.

The afterslip distribution was inverted using the steepest descent method. Prior to the inversion, the cumulative postseismic deformation was downsampled using a quadtree algorithm⁴³ (Fig. S11). Since afterslip typically occurs around the coseismic rupture, the fault plane of the DMCF is extended along the dip direction to a depth of 30 km to account for potential deep afterslip. Furthermore, given the predominantly normal-faulting mechanism of the Dingri earthquake, we constrained the rake angle of postseismic slip to 225°–315°. To account for potential long-wavelength deformation signals caused by viscoelastic relaxation in the postseismic observations, we first removed the estimated viscoelastic deformation using the aforementioned viscoelastic relaxation model before inverting the residual deformation for afterslip distribution. Similar to the procedure used for quantifying the uncertainty of the coseismic slip model, we employed the Jackknife resampling method⁴⁷ to evaluate the uncertainty of the afterslip model (Fig. S21). For comparison, we also conducted a separate inversion directly using the cumulative postseismic deformation without

removing the viscoelastic component, thereby obtaining the afterslip distribution that does not consider the contribution from viscoelastic relaxation (Fig. S16).

Data availability

The optical satellite image is sourced from the online map provided by ESRI Corporation (<https://www.arcgis.com/>). The LuTan-1 data were provided by the China Centre for Resources Satellite Data and Application. Sentinel-1 data used in this study were downloaded from the Alaska Satellite Facility (<https://search.asf.alaska.edu/>) and are provided by the European Space Agency as part of the Copernicus Programme. GACOS data is available at (<http://www.gacos.net/>). SRTM DEM can be downloaded from (<https://opentopography.org/>). The Gaofen series imagery can be accessed from <https://www.ncdc.ac.cn/portal/emergency?eid=34960ecc-bf9f-424a-8536-6b7fdbf942cc>. All teleseismic data were downloaded from the IRIS Wilber 3 system (<https://ds.iris.edu/wilber3/>). The aftershock catalog was downloaded from <https://zenodo.org/records/14784279>. The MATLAB code of BP is available at <https://github.com/lsmeng/MUSICBP>. The coseismic and postseismic deformation data and associated models are available in a data repository (<https://doi.org/10.5281/zenodo.17394099>).

Received: 8 August 2025; Accepted: 11 December 2025;

Published online: 26 December 2025

References

- Shi, F. et al. Seismogenic fault and coseismic surface deformation of the Dingri Ms6.8 earthquake in Xizang, China. *Seismol. Geol.* **47**, 1–15 (2025).
- Zou, J. et al. Surface rupture interpretation and building damage assessment of Xizang Dingri Ms6.8 earthquake on January 7, 2025. *Seismol. Geol.* **47**, 16–35 (2025).
- Yu, C. et al. Source parameters and induced hazards of the 2025 Mw 7.1 Dingri Earthquake on the Southern Tibetan Plateau (Xizhang), China, as Revealed by Imaging Geodesy. *J. Earth Sci.* **36**, 847–851 (2025).
- Yao, J. et al. A preliminary catalog of early aftershocks following the 7 January 2025 MS6.8 Dingri, Xizang Earthquake. *J. Earth Sci.* **36**, 856–860 (2025).
- Liu, Q. et al. Geodetic observations and seismogenic structures of the 2025 Mw 7.0 Dingri Earthquake: the largest normal faulting event in the Southern Tibet Rift. *Remote Sens.* **17**, 1096 (2025).
- Qiao, X. et al. The 2025 M_w 7.0 Dingri Earthquake: conjugate normal faulting of a graben structure in the southern Xainza-Dinggye Rift. *Geophys. Res. Lett.* **52**, e2025GL116154 (2025).
- Yang, J., Wen, Y., Xu, C. & Hu, Q. Complex multifault rupture during the 2016–2025 dingri earthquakes, southern Tibetan Plateau, unraveled by multisource InSAR Observations. *Seismol. Res. Lett.* (2025).
- Molnar, P. & Tapponnier, P. Cenozoic tectonics of Asia: effects of a continental collision. *Science* **189**, 419–426 (1975).
- Tapponnier, P., Mercier, J. L., Armijo, R., Tonglin, H. & Ji, Z. Field evidence for active normal faulting in Tibet. *Nature* **294**, 410–414 (1981).
- Wang, Q. et al. Present-day crustal deformation in China constrained by Global Positioning System measurements. *Science* **294**, 574–577 (2001).
- Zhang, P. et al. Continuous deformation of the Tibetan Plateau from global positioning system data. *Geology* **32**, 809–812 (2004).
- Yin, A. & Harrison, T. M. Geologic evolution of the Himalayan-Tibetan Orogen. *Annu. Rev. Earth Planet. Sci.* **28**, 211–280 (2000).
- Chen, H. et al. Large-scale extensional strain in Southern Tibet from Sentinel-1 InSAR and GNSS data. *Geophys. Res. Lett.* **51**, e2024GL110512 (2024).
- Royden, L. H., Burchfiel, B. C. & van der Hilst, R. D. The Geological Evolution of the Tibetan Plateau. *Science* **321**, 1054–1058 (2008).

15. Royden, L. H. et al. Surface deformation and lower crustal flow in Eastern Tibet. *Science* **276**, 788–790 (1997).
16. Clark, M. K. & Royden, L. H. Topographic ooze: building the eastern margin of Tibet by lower crustal flow. *Geology* **28**, 703–706 (2000).
17. Bai, D. et al. Crustal deformation of the eastern Tibetan plateau revealed by magnetotelluric imaging. *Nat. Geosci.* **3**, 358–362 (2010).
18. Tapponnier, P., Peltzer, G., Le Dain, A. Y., Armijo, R. & Cobbold, P. Propagating extrusion tectonics in Asia: New insights from simple experiments with plasticine. *Geology* **10**, 611–616 (1982).
19. Harrison, T. M., Copeland, P., Kidd, W. S. F. & Yin, A. Raising Tibet. *Science* **255**, 1663–1670 (1992).
20. Tian, T. & Wu, Z. Recent prehistoric major earthquake event of Dingmucuo Normal fault in the southern segment of Shenzha-Dingjie Rift and its seismic geological significance. *Geol. Rev.* **69**, 53–55 (2023).
21. Hu, J., Li, Z., Zhu, J., Ren, X. & Ding, X. Inferring three-dimensional surface displacement field by combining SAR interferometric phase and amplitude information of ascending and descending orbits. *Sci. China Earth Sci.* **53**, 550–560 (2010).
22. Xu, W. et al. Space geodetic evidence of basement-involved thick-skinned orogeny and fault frictional heterogeneity of the Papuan Fold Belt, Papua New Guinea. *J. Geophys. Res. Solid Earth* **127**, e2022JB024227 (2022).
23. Liu, J., Jónsson, S., Li, X., Yao, W. & Klinger, Y. Extensive off-fault damage around the 2023 Kahramanmaraş earthquake surface ruptures. *Nat. Commun.* **16**, 1286 (2025).
24. Fialko, Y., Sandwell, D., Simons, M. & Rosen, P. Three-dimensional deformation caused by the Bam, Iran, earthquake and the origin of shallow slip deficit. *Nature* **435**, 295–299 (2005).
25. Marone, C. J., Scholtz, C. H. & Bilham, R. On the mechanics of earthquake afterslip. *J. Geophys. Res. Solid Earth* **96**, 8441–8452 (1991).
26. Liu, X. & Xu, W. Logarithmic model joint inversion method for coseismic and postseismic slip: application to the 2017 Mw 7.3 Sarpol Zahāb Earthquake, Iran. *J. Geophys. Res. Solid Earth* **124**, 12034–12052 (2019).
27. Kaneko, Y. & Fialko, Y. Shallow slip deficit due to large strike-slip earthquakes in dynamic rupture simulations with elasto-plastic off-fault response. *Geophys. J. Int.* **186**, 1389–1403 (2011).
28. Xu, X. et al. Refining the shallow slip deficit. *Geophys. J. Int.* **204**, 1867–1886 (2016).
29. Guo, R. et al. Seismic versus aseismic slip for the 2023 Kahramanmaraş earthquake doublet. *Nat. Commun.* **16**, 959 (2025).
30. Yao, J. et al. A preliminary early aftershock catalog for the 2025 Ms6.8 Dingri earthquake. *Zenodo* <https://zenodo.org/records/14784279> (2025).
31. Liu, C. et al. Kilometer-resolution three-dimensional crustal deformation of Tibetan Plateau from InSAR and GNSS. *Sci. China Earth Sci.* **67**, 1818–1835 (2024).
32. Taylor, M. & Yin, A. Active structures of the Himalayan-Tibetan orogen and their relationships to earthquake distribution, contemporary strain field, and Cenozoic volcanism. *Geosphere* **5**, 199–214 (2009).
33. Yin, A. & Taylor, M. H. Mechanics of V-shaped conjugate strike-slip faults and the corresponding continuum mode of continental deformation. *GSA Bull.* **123**, 1798–1821 (2011).
34. Wang, M. & Shen, Z. Present-day crustal deformation of continental China derived from GPS and its tectonic implications. *J. Geophys. Res. Solid Earth* **125**, e2019JB018774 (2020).
35. Styron, R. H., Taylor, M. H. & Murphy, M. A. Oblique convergence, arc-parallel extension, and the role of strike-slip faulting in the High Himalaya. *Geosphere* **7**, 582–596 (2011).
36. Tang, X. et al. In-orbit application parameters test and analysis of L-band differential interferometric SAR satellite constellation. *Acta Geod. Cartogr. Sin.* **53**, 1863–1872 (2024).
37. Werner, C., Wegmüller, U., Strozzi, T. & Wiesmann, A. in *Proceedings of the ers-ensat symposium, Gothenburg, Sweden*. Vol. 1620 (Citeseer, 2000).
38. Xu, W. et al. Transpressional rupture cascade of the 2016 Mw 7.8 Kaikoura Earthquake, New Zealand. *J. Geophys. Res. Solid Earth* **123**, 2396–2409 (2018).
39. Farr, T. G. & Kobrick, M. Shuttle radar topography mission produces a wealth of data. *Eos, Trans. Am. Geophys. Union* **81**, 583–585 (2000).
40. Goldstein, R. M. & Werner, C. L. Radar interferogram filtering for geophysical applications. *Geophys. Res. Lett.* **25**, 4035–4038 (1998).
41. Chen, C. W. & Zebker, H. A. Phase unwrapping for large SAR interferograms: statistical segmentation and generalized network models. *IEEE Trans. Geosci. Remote Sens.* **40**, 1709–1719 (2002).
42. Michel, R., Avouac, J.-P. & Taboury, J. Measuring ground displacements from SAR amplitude images: application to the Landers Earthquake. *Geophys. Res. Lett.* **26**, 875–878 (1999).
43. Jónsson, S., Zebker, H., Segall, P. & Amelung, F. Fault slip distribution of the 1999 Mw 7.1 Hector Mine, California, Earthquake, estimated from satellite radar and GPS measurements. *Bull. Seismol. Soc. Am.* **92**, 1377–1389 (2002).
44. Okada, Y. Surface deformation due to shear and tensile faults in a half-space. *Bull. Seismol. Soc. Am.* **75**, 1135–1154 (1985).
45. Wang, R. et al. The 2011 Mw 9.0 Tohoku Earthquake: comparison of GPS and strong-motion data. *Bull. Seismol. Soc. Am.* **103**, 1336–1347 (2013).
46. Zhang, Y. et al. The 2009 L'Aquila MW 6.3 earthquake: a new technique to locate the hypocentre in the joint inversion of earthquake rupture process. *Geophys. J. Int.* **191**, 1417–1426 (2012).
47. Melgar, D. et al. Seismogeodesy of the 2014 M6.1 Napa earthquake, California: rapid response and modeling of fast rupture on a dipping strike-slip fault. *J. Geophys. Res. Solid Earth* **120**, 5013–5033 (2015).
48. Meng, L., Inbal, A. & Ampuero, J.-P. A window into the complexity of the dynamic rupture of the 2011 Mw 9 Tohoku-Oki earthquake. *Geophys. Res. Lett.* **38**, L00G07 (2011).
49. Berardino, P., Fornaro, G., Lanari, R. & Sansosti, E. A new algorithm for surface deformation monitoring based on small baseline differential SAR interferograms. *IEEE Trans. Geosci. Remote Sens.* **40**, 2375–2383 (2002).
50. Biggs, J., Wright, T., Lu, Z. & Parsons, B. Multi-interferogram method for measuring interseismic deformation: Denali Fault, Alaska. *Geophys. J. Int.* **170**, 1165–1179 (2007).
51. Yu, C., Li, Z. & Penna, N. T. Interferometric synthetic aperture radar atmospheric correction using a GPS-based iterative tropospheric decomposition model. *Remote Sens. Environ.* **204**, 109–121 (2018).
52. Jónsson, S., Segall, P., Pedersen, R. & Björnsson, G. Post-earthquake ground movements correlated to pore-pressure transients. *Nature* **424**, 179–183 (2003).
53. Bürgmann, R. & Dresen, G. Rheology of the lower crust and upper mantle: evidence from rock mechanics, geodesy, and field observations. *Annu. Rev. Earth Planet. Sci.* **36**, 531–567 (2008).
54. Wang, K. & Bürgmann, R. Probing fault frictional properties during afterslip updip and downdip of the 2017 Mw 7.3 Sarpol-e Zahab earthquake with space geodesy. *J. Geophys. Res. Solid Earth* **125**, e2020JB020319 (2020).
55. Peltzer, G., Rosen, P., Rogez, F. & Hudnut, K. Poroelastic rebound along the Landers 1992 earthquake surface rupture. *J. Geophys. Res. Solid Earth* **103**, 30131–30145 (1998).
56. Zhang, J., Zhao, B., Wang, D., Yu, J. & Tan, K. Dynamic modeling of postseismic deformation following the 2015 Mw 7.8 Gorkha earthquake, Nepal. *J. Asian Earth Sci.* **215**, 104781 (2021).
57. Tian, Z., Freymueller, J. T. & Yang, Z. Spatio-temporal variations of afterslip and viscoelastic relaxation following the Mw 7.8 Gorkha (Nepal) earthquake. *Earth Planet. Sci. Lett.* **532**, 116031 (2020).
58. Diao, F., Wang, R., Xiong, X. & Liu, C. Overlapped postseismic deformation caused by afterslip and viscoelastic relaxation following the 2015 Mw 7.8 Gorkha (Nepal) Earthquake. *J. Geophys. Res. Solid Earth* **126**, e2020JB020378 (2021).
59. Wang, R., Lorenzo-Martín, F. & Roth, F. PSGRN/PSCMP—a new code for calculating co- and post-seismic deformation, geoid and

- gravity changes based on the viscoelastic-gravitational dislocation theory. *Computers Geosci.* **32**, 527–541 (2006).
60. Laske, G., Masters, G., Ma, Z. & Pasyanos, M. Update on CRUST1.0 - A 1-degree Global Model of Earth's Crust. *Geophys. Res. Abstracts.* **15** (2013).
61. Zelenin, E., Bachmanov, D., Garipova, S., Trifonov, V. & Kozhurin, A. in *Earth Syst. Sci. Data* Vol. 14 4489-4503 (Copernicus Publications, 2022).

Acknowledgements

This research was supported by National Natural Science Foundation of China (42388102, 42174023, 42304037), Natural Science Foundation of Hunan Province (2024JJ3031), National Key Research and Development Program (2022YFB3903602). We acknowledge the use of ENVI (Version 5.6) software in optical satellite image processing. The figures were prepared using the public domain Generic Mapping Tools (version 6.4.0), MATLAB (version R2021b) and QGIS (version 3.34).

Author contributions

Wenbin Xu 'contributed' Conceptualization, Methodology, Investigation, Visualization, Supervision and Writing. Chengyuan Bai 'contributed' Investigation, Visualization and Writing. Chuanchao Huang 'contributed' Investigation and Writing. Roland Bürgmann 'contributed' Methodology and Writing. Baojun Shan 'contributed' Investigation. Xinjian Shan 'contributed' Writing. Zhidan Chen 'contributed' Investigation. Lei Xie 'contributed' Investigation. Feng Shi 'contributed' investigation.

Competing interests

The authors declare no competing interests.

Additional information

Supplementary information The online version contains supplementary material available at <https://doi.org/10.1038/s43247-025-03132-0>.

Correspondence and requests for materials should be addressed to Wenbin Xu.

Peer review information *Communications Earth and Environment* thanks Meike D. W. Scherrenberg and the other anonymous reviewer(s) for their contribution to the peer review of this work. Primary Handling Editors: Carlos Vargas and Alireza Bahadori. A peer review file is available.

Reprints and permissions information is available at <http://www.nature.com/reprints>

Publisher's note Springer Nature remains neutral with regard to jurisdictional claims in published maps and institutional affiliations.

Open Access This article is licensed under a Creative Commons Attribution-NonCommercial-NoDerivatives 4.0 International License, which permits any non-commercial use, sharing, distribution and reproduction in any medium or format, as long as you give appropriate credit to the original author(s) and the source, provide a link to the Creative Commons licence, and indicate if you modified the licensed material. You do not have permission under this licence to share adapted material derived from this article or parts of it. The images or other third party material in this article are included in the article's Creative Commons licence, unless indicated otherwise in a credit line to the material. If material is not included in the article's Creative Commons licence and your intended use is not permitted by statutory regulation or exceeds the permitted use, you will need to obtain permission directly from the copyright holder. To view a copy of this licence, visit <http://creativecommons.org/licenses/by-nc-nd/4.0/>.

© The Author(s) 2025